

Classically entangled optical beams for high-speed kinematic sensing

Stefan Berg-Johansen,^{1,2} Falk Töppel,^{1,2,3} Birgit Stiller,^{1,2} Peter Banzer,^{1,2,4} Marco Ornigotti,⁵
 Elisabeth Giacobino,^{1,6} Gerd Leuchs,^{1,2,4} Andrea Aiello,^{1,2} and Christoph Marquardt^{1,2}

¹Max Planck Institute for the Science of Light, Günther-Scharowsky-Straße 1/Bldg. 24, 91058 Erlangen, Germany

²Institute for Optics, Information and Photonics, Universität Erlangen-Nürnberg, Staudtstraße 7/B2, 91058 Erlangen, Germany

³Erlangen Graduate School in Advanced Optical Technologies (SAOT), Paul-Gordan-Straße 6, 91052 Erlangen, Germany

⁴Department of Physics, University of Ottawa, 25 Templeton, Ottawa, Ontario, K1N 6N5 Canada

⁵Institute of Applied Physics, Friedrich-Schiller University Jena, Max-Wien Platz 1, 07743 Jena, Germany

⁶Laboratoire Kastler Brossel, Université Pierre et Marie Curie, École Normale Supérieure, CNRS, 4 place Jussieu, 75252 Paris, France

(Dated: December 3, 2024)

Tracking the kinematics of fast-moving objects is an important diagnostic tool for science and engineering. Existing optical methods include high-speed CCD/CMOS imaging [1], streak cameras [2], lidar [3], serial time-encoded imaging [4] and sequentially timed all-optical mapping [5]. Here, we demonstrate an entirely new approach to positional and directional sensing based on the concept of *classical entanglement* [6–8] in vector beams of light. The measurement principle relies on the intrinsic correlations existing in such beams between transverse spatial modes and polarization. The latter can be determined from intensity measurements with only a few fast photodiodes, greatly outperforming the bandwidth of current CCD/CMOS devices. In this way, our setup enables two-dimensional real-time sensing with temporal resolution in the GHz range. We expect the concept to open up new directions in photonics-based metrology and sensing.

Vector beams of light with cylindrical, non-uniform polarization patterns [9] have found application in diverse areas of optics such as improved focusing [10–12], laser machining [13, 14], plasmon excitation [15], metrology [16], optical trapping [17] and nano-optics [18–20]. Recently, vector beams have attracted attention [21–26] due to a simple but striking property: when viewed as a superposition of transverse electromagnetic modes with orthogonal linear polarizations, the nonseparable mode function of a radially polarized vector beam is mathematically equivalent to a maximally entangled Bell state of two qubits known from quantum mechanics [27]. In contrast with the canonical Bell states in quantum optics, where two photons are entangled in polarization and exhibit non-local correlations when spatially separated, this “classical entanglement” in vector beams is necessarily local as it exists only between different degrees of freedom of one and the same physical system [28].

However, these correlations have recently been shown to represent a valuable resource. Vector beams have been used to violate an analogue of Bell’s inequality for spin-orbit modes [23, 24] and have led to continuous-variable entanglement between different degrees of freedom [29]. In addition, vector beams have been used to

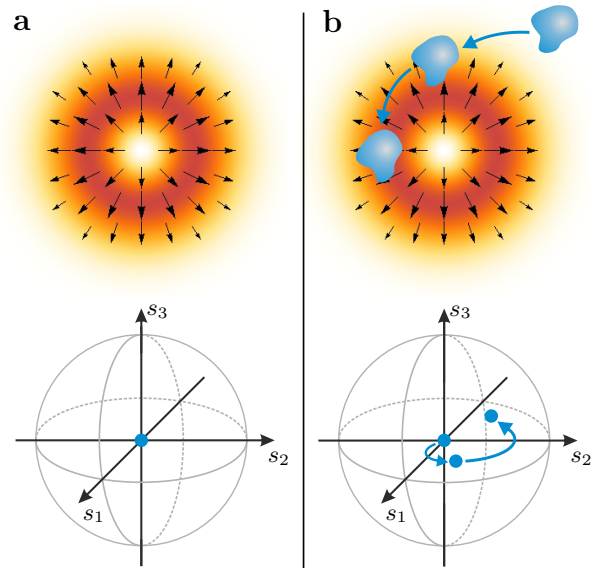


FIG. 1. **Classical entanglement.** **a.** (top) The transverse electric field distribution of a radially polarized beam of light. The orange density plot shows the beam’s doughnut-shaped intensity distribution, while black arrows indicate the position-dependent instantaneous local direction of the electric field vector. (bottom) The beam’s global polarization state is shown in a Poincaré sphere representation. Initially, the light field is globally unpolarized, with the Poincaré vector located at the origin. **b.** If an opaque obstacle is brought into the beam, the global polarization takes on non-zero values according to the position of the obstacle within the beam. This method allows the kinematics of the object to be inferred from a polarization measurement alone.

implement classical counterparts of quantum protocols [30, 31]. Promising proposals include an application to the study of quantum random walks [32] and real-time single-shot Mueller matrix measurements [33]. In the present work, we demonstrate for the first time a fully operational application of classical entanglement to high-speed kinematic sensing.

Several techniques are nowadays available for sensing the kinematics of fast-moving objects [1–5]. Each comes with its own strengths and drawbacks. For example, high-speed imaging is typically limited to capturing

only a small number of frames, while pump-probe techniques require the recorded event to be repeated identically many times. Ideally, one seeks a solution that is capable of performing fast sensing continuously, in real-time and from a simple setup, employing only standard equipment and offering flexibility in the choice of wavelength. By using the nonseparable mode structure of cylindrically polarized beams (see Figure 1), one only needs to detect changes in polarization, thus fulfilling all the above requirements at the same time. In the following, we first discuss the physics of vector beams and then introduce the technique of sensing and show the results of our experimental investigations.

The electric field of a general non-uniformly polarized paraxial beam can be written as:

$$\mathbf{E}(\boldsymbol{\rho}, z) = \mathbf{e}_1 f_1(\boldsymbol{\rho}, z) + \mathbf{e}_2 f_2(\boldsymbol{\rho}, z), \quad (1)$$

where the vectors $\mathbf{e}_1, \mathbf{e}_2$ determine the polarization of the beam, the scalar functions $f_1(\boldsymbol{\rho}, z), f_2(\boldsymbol{\rho}, z)$ set the wavefront and $\boldsymbol{\rho} = \hat{\mathbf{x}}x + \hat{\mathbf{y}}y$ is the transverse position vector (see ‘‘Methods’’ below). The expression (1) is *nonseparable*, namely it is not possible to rewrite it as the simple product of only one polarization vector and a single scalar function. In this sense, Eq. (1) has the same mathematical structure as a two-qubit entangled quantum state [28]. It is a well-established result of mathematical physics that any two-dimensional field of the form (1) can be recast in the so-called Schmidt form $\mathbf{E}(\boldsymbol{\rho}, z) = \sqrt{\lambda_1} \hat{\mathbf{u}}_1 v_1(\boldsymbol{\rho}, z) + \sqrt{\lambda_2} \hat{\mathbf{u}}_2 v_2(\boldsymbol{\rho}, z)$ where $\{\hat{\mathbf{u}}_1, \hat{\mathbf{u}}_2\}$ and $\{v_1, v_2\}$ form complete orthonormal bases in the polarization and spatial mode vector spaces, respectively, with $\lambda_1 \geq \lambda_2 \geq 0$. If either $\lambda_1 = 0$ or $\lambda_2 = 0$, the expression of $\mathbf{E}(\boldsymbol{\rho}, z)$ is factorable and the beam is uniformly polarized. Vice versa, if $\lambda_1 \lambda_2 \neq 0$, the beam displays a non-uniform polarization pattern and is said to be ‘‘classically entangled’’. Thus, analogously to a bona fide quantum state, in a non-uniformly polarized beam, polarization and spatial degrees of freedom are so strongly correlated that if, by any means, one alters the spatial profile of the beam, then the polarization changes accordingly. Our sensing technique relies precisely upon this peculiar phenomenon. Owing to the classical entanglement exhibited by the beam, we are able to retrieve information about the position of a moving object partially obstructing the beam only by measuring the polarization of the latter: no spatially resolving measurements are needed. Since polarization measurements can be performed at GHz rates, with our system we are able to track very fast objects.

For a field $\mathbf{E}(\boldsymbol{\rho}, z)$ in the Schmidt form, the measurable Stokes parameters can be written as

$$s_0 = \lambda_1 + \lambda_2, \quad (2a)$$

$$s_1 = (\lambda_1 - \lambda_2)(|a_x|^2 - |a_y|^2), \quad (2b)$$

$$s_2 = (\lambda_1 - \lambda_2)(a_x a_y^* + a_x^* a_y), \quad (2c)$$

$$s_3 = i(\lambda_1 - \lambda_2)(a_x a_y^* - a_x^* a_y), \quad (2d)$$

where $a_x = \hat{\mathbf{u}}_1 \cdot \hat{\mathbf{x}}$ and $a_y = \hat{\mathbf{u}}_1 \cdot \hat{\mathbf{y}}$. In a radially polarized beam one has $\lambda_1 = \lambda_2$ and thus $s_1 = s_2 = s_3 = 0$, reflecting the fact that such a beam appears completely unpolarized in the absence of an obstruction [34].

When an *opaque* object cuts across a non-uniformly polarized beam, the spatial/polarization pattern of the latter varies with time according to the instantaneous position of the obstructing object, as described by its central coordinates $x_0(t), y_0(t)$. It is not difficult to show that for such a modified beam, Eqs. (2) are still valid, provided that $\lambda_1, \lambda_2, a_x, a_y$ are regarded now as functions of $x_0(t), y_0(t)$. When the values of the Stokes parameters s_0, s_1, s_2, s_3 are replaced by the measured ones on the left side of Eqs. (2), these can be regarded as a nonlinear algebraic system of four equations for the two variables $x_0(t), y_0(t)$, which can be solved by means of suitable algorithms. In this way, the instantaneous trajectory of the object is recovered.

The experimental setup is shown in Figure 2. We prepare a continuous-wave laser beam in a radially polarized mode. The beam impinges on a moving sample. Subsequently, half-waveplates and polarizing beam splitters are used to project the beam onto its horizontal, vertical, diagonal and anti-diagonal polarization components. Finally, a network of four InGaAs photodetectors with 4 GHz 3 dB-bandwidth measures the individual projections, from which the Stokes parameters s_0, s_1 and s_2 can be straightforwardly obtained (see ‘‘Methods’’). For the particular case of a radially polarized mode, the s_3 parameter is always zero. An auxiliary camera is used for additional visual verification and beam characterization.

In order to demonstrate the broad applicability of the system, three types of measurement are carried out. First, a metal rotor is made to turn about the centre of the beam (Figure 3a). By sampling the Stokes parameters during the motion of the rotor, the instantaneous value of its angle of rotation θ_0 is successfully inferred. An accuracy of 4.1° (mean error) is achieved without correcting for imperfections of the beam and detector coupling.

Second, a metal sphere is moved across the beam (Figure 3b). We measure the Stokes parameters with an acquisition time of 250 ps at each position. A Bayesian algorithm is used to estimate the sphere’s position from these data (see Supplementary Material). The inferred trajectory shown in Figure 3b is seen to be in good agreement with the actual trajectory. As one expects, the inference is particularly successful in areas where the beam has a high intensity, i.e. where the Stokes parameter modulation introduced by the sphere results in a higher signal-to-noise ratio.

Third and finally, the real-time capability of the method is demonstrated by measuring the transit of a metal blade moving at 32 m s^{-1} across the beam. The event is captured as a sequence of single-shot measurements, requiring only a single occurrence of the event. The measurement is triggered on a change in s_0 , meaning that the particular instant of an event does not have to be known in advance. Figure 4 shows the captured

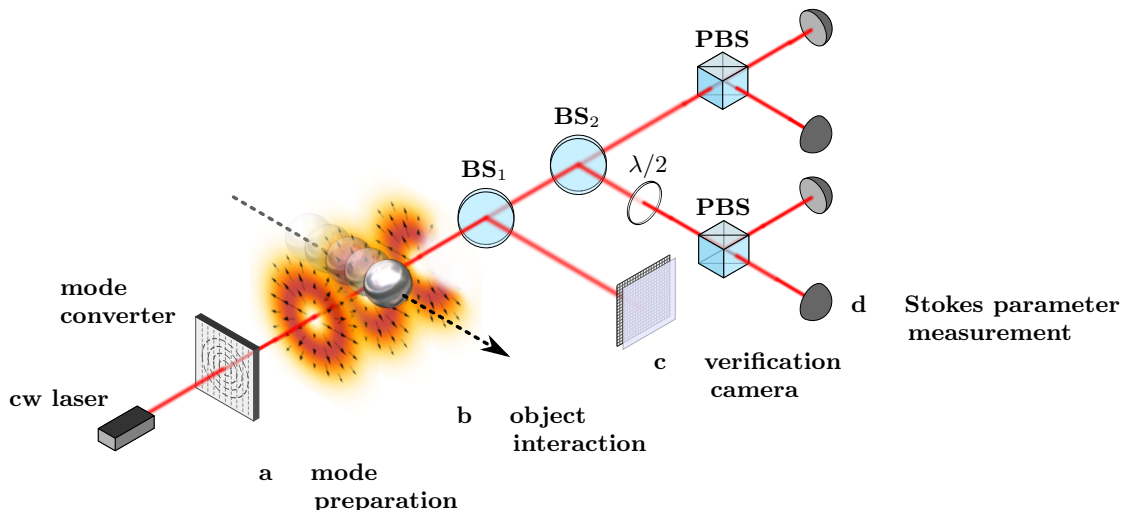


FIG. 2. **Experimental setup.** **a.** A continuous-wave laser beam is prepared in a radially polarized mode by a liquid crystal mode converter. **b.** The beam impinges on an opaque object whose motion in space modulates the beam’s polarization Stokes parameters. **c.** A polarization-independent beamsplitter (BS1) taps off 10% of the beam for inspection by a conventional camera. This allows for characterization of the mode pattern and independent verification measurements. **d.** A polarization-independent 50/50 beamsplitter (BS2) divides the beam up for projection onto its linear polarization components via a pair of polarizing beamsplitters (PBS) and a half-wave plate ($\lambda/2$). The projections are simultaneously measured by four InGaAs detectors with 4 GHz bandwidth. By linear combination of the projection signals, the beam’s Stokes parameters are obtained. Knowledge of the Stokes parameters allows the instantaneous trajectory of the sample to be reconstructed (see Figure 3).

data. The event lasts for 200 μs , after which the beam is fully covered. Since the Stokes parameters are captured continuously there is no dead time. For each measured Stokes parameter, 10^6 individual samples are acquired for a single event, reflecting the fact that the temporal resolution provided by the detection apparatus far exceeds the time scale of the blade’s motion.

All three measurements confirm the system’s ability to perform quantitatively meaningful kinematic sensing at very high temporal resolutions. The measurement precision is subject to random error from the electronic noise of the detectors at high bandwidths. This becomes dominant in the regime where the measured sample has only a small overlap with the beam (as seen in Figure 3b), or when the sample covers the beam completely. Some applications, such as precision sensing of objects moving within a confined region, may benefit from using a beam with a nonzero s_3 Stokes parameter. Such beams have been suggested for the investigation of small particle scattering [35]. Although they require an additional photodiode pair, such beams avoid the zero of intensity at the origin. We note, however, that the classical entanglement of such a beam is not maximal, and that the correlations between polarization and position are therefore necessarily weaker.

In summary, we have demonstrated that the classical entanglement manifested by vector beams of light may be used to detect the kinematics of very fast objects with GHz temporal bandwidth. The method is possible because for cylindrically polarized beams, spatial

information may be acquired by measurements on the polarization degree of freedom, owing to their classically entangled mode structure. The method presented requires only standard optical components which are commercially available at a wide range of optical wavelengths and can easily be extended to the microwave regime. It allows for continuous, real-time measurement of 2D spatial information with unprecedented temporal resolution. We suggest that due to its simplicity, the method may even be employed in noisy environments such as free-space channels. For example, existing lidar technologies based on time-of-flight measurements may be enhanced by the new method. On the microscale, focused classically entangled modes may provide a new approach to precision measurements, for example of Brownian motion in the ballistic regime [36].

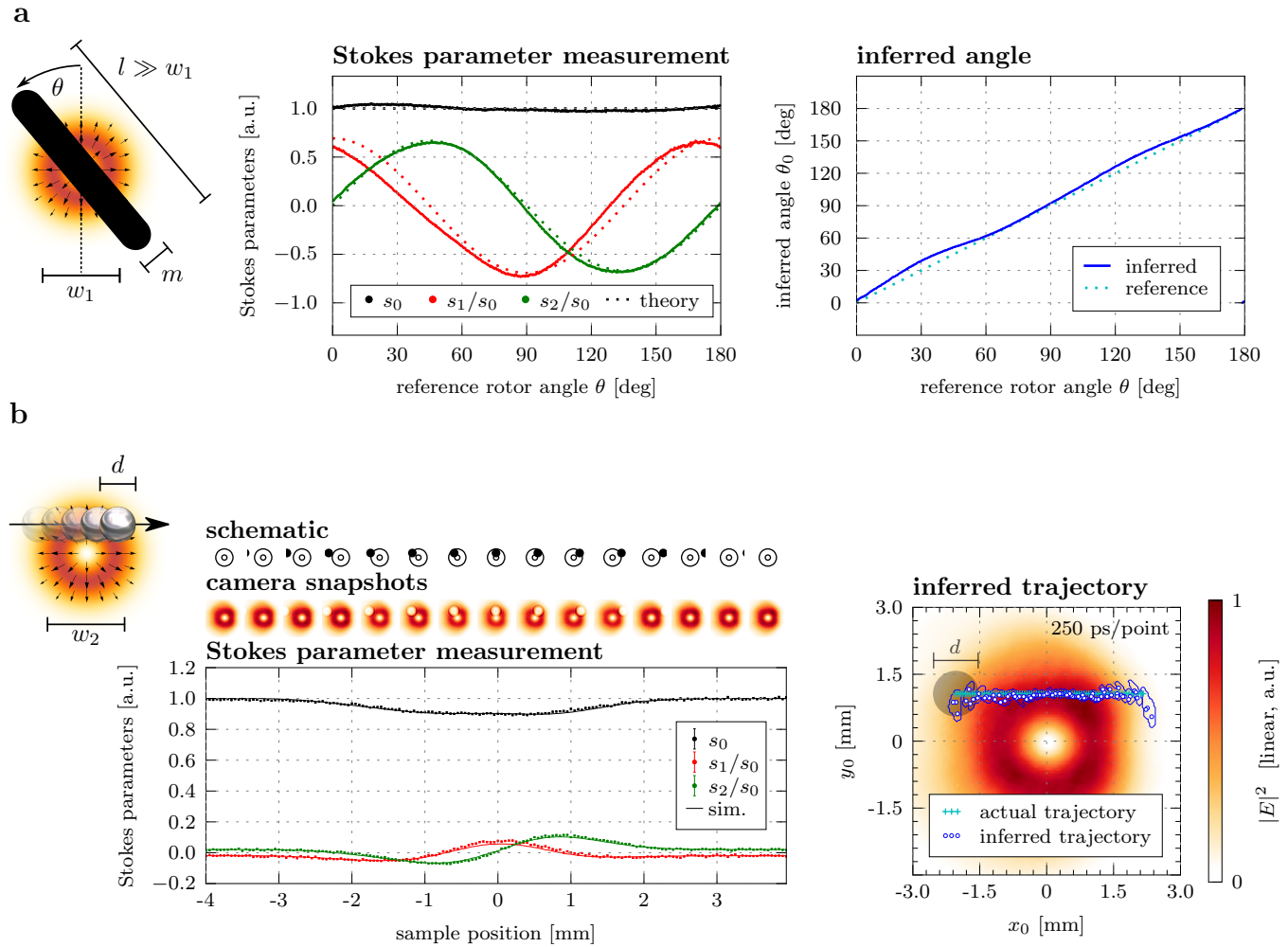


FIG. 3. Rotation sensing and position tracking. **a.** A metal rotor (width $m = 0.79(1)$ mm) turns about the centre of a radially polarized beam (width $w_1 = 1.95(10)$ mm). Due to the classically entangled structure of the beam, the rotation in space induces a sinusoidal oscillation of the beam's Stokes parameters. Measurements of the s_0 , s_1 and s_2 Stokes parameters allow the instantaneous angle of rotation to be inferred. Each data point was obtained by integrating over 200 ns, so that electronic noise is averaged out to within the width of the points. Dotted curves show the theoretically expected values under the assumption of an ideal mode function. **b.** (*left*) A metal sphere (diameter $d = 1.00(1)$ mm) traverses a radially polarized light beam (width $w_2 = 2.84(10)$ mm). (*center*) The Stokes parameters s_0 , s_1 and s_2 vary as a function of the sphere's position. Solid lines show the expected Stokes parameters as obtained from simulation. (*right*) The trajectory of the sphere is inferred from the measured Stokes parameters. The sphere is moved gradually in discrete steps of $50 \mu\text{m}$, providing a calibrated, reproducible reference motion. To allow for a realistic comparison with a fast object, the acquisition time at each point is only 250 ps. The blue contours show the combined Bayesian 68% credible region R , while the gray shadow shows the dimensions of the sphere to scale. The theoretical model used to obtain the theory and simulation curves for a and b, respectively, is detailed in the "Methods" section. The position tracking algorithm is described in detail in the Supplementary Material. In both plots, s_0 is normalised to its initial value, while s_1 and s_2 are normalised to the instantaneous value of s_0 .

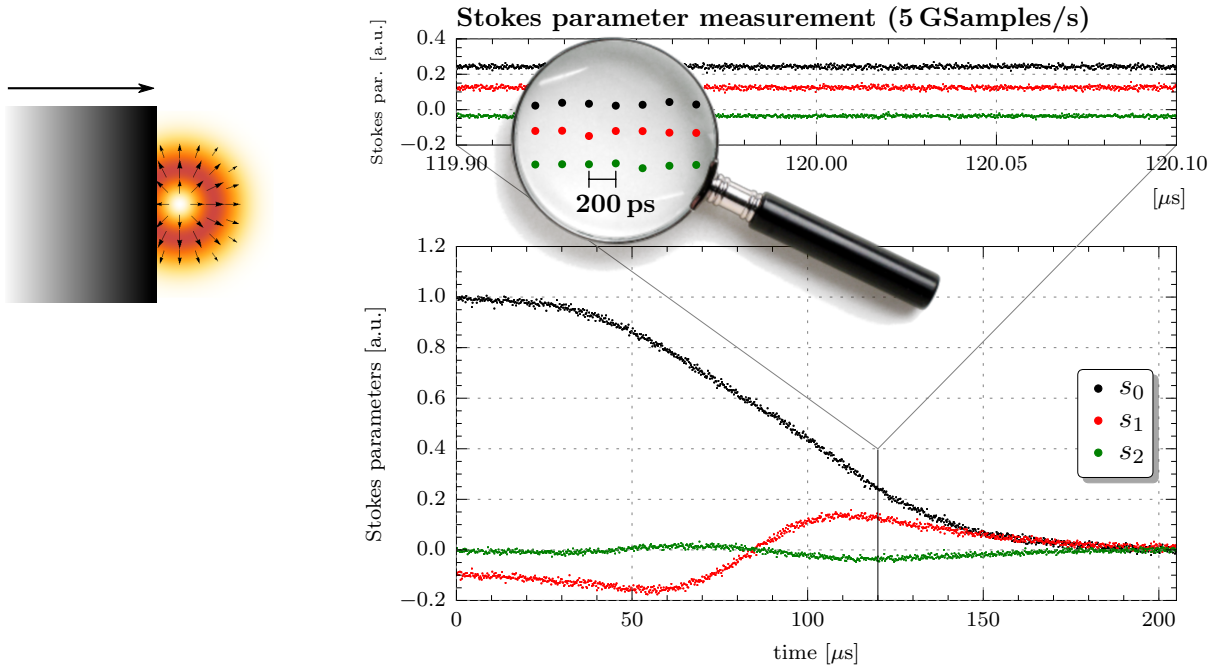


FIG. 4. **Real-time sensing.** A metal blade cuts across a radially polarized mode (width $w_2 = 2.84(10)$ mm) at 32 m s^{-1} . The plot shows a sequence of single-shot measurements of the beam's s_0 , s_1 and s_2 Stokes parameters during the passage of the blade until the beam is fully covered, normalised to the initial intensity. The temporal resolution reaches up to 200 ps.

Methods

Experimental setup. We employed a continuous-wave diode laser (Sumitomo SLT5411) with wavelength $\lambda = 1550$ nm, amplified by an erbium-doped fiber amplifier (OPREL OFA20-1231S) to a power of 50 mW. The initially Gaussian beam profile was converted to a radial mode using a commercially available liquid crystal device (Arcoptix S.A.) with custom anti-reflection coatings. The mode then passed two further waveplates in order to suppress residual circular polarization components resulting from the mode converter. The rotor was a Cu-coated wire of width 0.79(1) mm, placed in a rotation mount which was actuated by a stepper motor. The sphere had diameter 1.00(1) mm and was made from steel. It was attached to an uncoated glass substrate of thickness 1 mm by a meniscus of epoxy resin which was small enough to be neglected optically. The substrate was mounted in a vertical position on a linear precision stage (PI M-410.DG, minimum incremental motion 0.1 μ m) and moved in steps of 50 μ m. The plane of object interaction was located at 50 cm after the mode converter. The distances between object-camera and object-detectors were 10 cm and 80 cm, respectively. The beam had a width of 2.84(10) mm in the plane of object interaction, and a Rayleigh range of approximately 2 m. All beam widths given here and in the main text are 90-10 knife-edge widths [37]. The detectors used to measure the horizontal, vertical, diagonal and anti-diagonal polarization components were two Soliton ET-3500, an Alphas UPD-35 and an Alphas UPD-70, respectively. The detectors were temporally matched to within 1.3 ns, with the remaining offset being compensated by the oscilloscope up to the measurement bandwidth. For the rotor measurement only, a pair of BPDV2120R fiber-coupled balanced photoreceivers with 43 GHz 3 dB-bandwidth from the company u²t were used. Tailored phase plates were used to convert the linearly polarized Hermite-Gauss projection modes into approximate fundamental modes in order to fiber-couple them to these detectors. All signals were recorded with a digital storage oscilloscope (Agilent DSO81204B in half-channel mode, 8 GHz analog bandwidth, sinc- x -interpolation disabled). An InGaAs camera with resolution 320 \times 256 px (Xenics XS) was used for beam inspection and for generating spatially resolved beam polarization tomographies prior to the actual sensing measurement. The Bayesian tracking algorithm described in the Supplementary Material used these tomographies in order to improve its estimate for the object position.

Theoretical model. In order to obtain the theoretical predictions and simulated values shown in Figure 3 we developed the following simple model. Consider a radially polarized beam of light of angular frequency ω , propagating along the z -axis of a Cartesian reference frame and polarized in the xy -plane. In the paraxial approximation its electric field takes the form $\mathbf{E}(\mathbf{r}, t) = \text{Re}[\mathbf{E}(\boldsymbol{\rho}, z) \exp(-i\omega t)]$ with time-independent mode function $\mathbf{E}(\boldsymbol{\rho}, z)$ (Jones vector). In the ideal case of a perfect radially polarized beam the mode function is given by

$$\mathbf{E}(\boldsymbol{\rho}, z) = \frac{1}{\sqrt{2}} [\hat{\mathbf{x}} \psi_{10}(\boldsymbol{\rho}, z) + \hat{\mathbf{y}} \psi_{01}(\boldsymbol{\rho}, z)]. \quad (3)$$

Therein $\psi_{mn}(\boldsymbol{\rho}, z)$, with $m, n \in \{0, 1, 2, \dots\}$, is the Hermite-Gaussian solution of the paraxial wave equation of order $N = m + n$ [38], while $\boldsymbol{\rho} = \hat{\mathbf{x}}x + \hat{\mathbf{y}}y$ denotes the transverse position vector. Please note that Eq. (3) is a particular case of the general expression in Eq. (1).

When an opaque obstacle is placed into the beam, covering a region \mathcal{A} in the xy -plane, the electric field directly behind the obstacle is given by

$$\mathbf{E}'(\boldsymbol{\rho}, z) = [1 - \mathcal{I}_{\mathcal{A}}(\boldsymbol{\rho})]\mathbf{E}(\boldsymbol{\rho}, z), \quad (4)$$

where

$$\mathcal{I}_{\mathcal{A}}(\boldsymbol{\rho}) = \begin{cases} 1 & \text{if } \boldsymbol{\rho} \in \mathcal{A}, \\ 0 & \text{if } \boldsymbol{\rho} \notin \mathcal{A}, \end{cases} \quad (5)$$

denotes the transmission function of the aperture complementary to the obstruction (Babinet's principle).

We are interested in the intensities of the perturbed beam after passing a linear polarizer making an angle $\varphi \in \{0^\circ, 90^\circ, 45^\circ, 135^\circ\}$ with the x -axis, as the Stokes parameters s_0, s_1, s_2 are easily calculated from these intensities. Representing Eqs. (3) and (4) as two-component Jones vectors and describing the action of the linear polarizer by the projection matrix

$$P_\varphi = \begin{bmatrix} \cos^2 \varphi & \sin \varphi \cos \varphi \\ \sin \varphi \cos \varphi & \sin^2 \varphi \end{bmatrix}$$

yields

$$\begin{aligned} I_{\mathcal{A}}(\varphi) &= \int |P_\varphi \mathbf{E}'(\boldsymbol{\rho}, z)|^2 d^2 \boldsymbol{\rho} \\ &= \int [1 - \mathcal{I}_{\mathcal{A}}(\boldsymbol{\rho})] |P_\varphi \mathbf{E}(\boldsymbol{\rho}, z)|^2 d^2 \boldsymbol{\rho} \end{aligned} \quad (6)$$

for the intensity of the beam behind the polarizer. With the help of Eq. (6), the Stokes parameters, measured in the plane of the obstructing object, take the form

$$s_0(\mathcal{A}) = I_{\mathcal{A}}(0^\circ) + I_{\mathcal{A}}(90^\circ), \quad (7a)$$

$$s_1(\mathcal{A}) = I_{\mathcal{A}}(0^\circ) - I_{\mathcal{A}}(90^\circ), \quad (7b)$$

$$s_2(\mathcal{A}) = I_{\mathcal{A}}(45^\circ) - I_{\mathcal{A}}(135^\circ), \quad (7c)$$

and are functions of \mathcal{A} , the region covered by the object within the beam. In simple cases, these equations may allow for straightforward algebraic inversion. To obtain the theoretical predictions shown in Figure 3a (rotor), we have used the time-independent mode function of the ideal radially polarized beam from Eq. (3). The rotation angle can then be obtained analytically as $\theta_0 = \arcsin(s_1/s_2)$. The simulated reference in Figure 3b (tracking) relies on experimentally measured distributions of $|P_\varphi \mathbf{E}(\boldsymbol{\rho}, z)|^2$ that have been substituted into Eq. (6). This allows for the numerical evaluation of a likelihood function L which is used by the position tracking algorithm (see Supplementary Material).

Acknowledgements

The authors would like to thank Tobias R othlingsh ofer for help with the experiment, Irina Harder for fabricating the phase plates, and Thomas Bauer for useful discussions.

-
- [1] Whybrew, A. High-speed imaging. In *Handbook of Laser Technology and Applications: Applications*, Sec. D2.7 (Institute of Physics Publishing, Bristol, 2004).
- [2] Velten, A., Raskar, R. & Bawendi, M. Picosecond camera for time-of-flight imaging. In *Imaging Systems and Applications*, IMB4 (Optical Society of America, 2011).
- [3] Weitkamp, C. *Lidar: Range-Resolved Optical Remote Sensing of the Atmosphere*. (Springer Series in Optical Sciences. Springer, New York, 2005).
- [4] Goda, K., Tsia, K. K. & Jalali, B. Serial time-encoded amplified imaging for real-time observation of fast dynamic phenomena. *Nature* **458**, 1145–1149 (2009).
- [5] Nakagawa, K. *et al.*. Sequentially timed all-optical mapping photography (STAMP). *Nat. Photonics* **8**, 695–700 (2014).
- [6] Spreeuw, R. J. C. A classical analogy of entanglement. *Found. Phys.* **28**, 361–374 (1998).
- [7] Spreeuw, R. J. C. Classical wave-optics analogy of quantum-information processing. *Phys. Rev. A* **63**, 062302 (2001).
- [8] Luis, A. Coherence, polarization, and entanglement for classical light fields. *Opt. Commun.* **282**, 3665–3670 (2009).
- [9] Zhan, Q. Cylindrical vector beams: From mathematical concepts to applications. *Adv. Opt. Photon.* **1**, 1–57 (2009).
- [10] Quabis, S., Dorn, R., Eberler, M., Glöckl, O. & Leuchs, G. Focusing light to a tighter spot. *Opt. Commun.* **179**, 1–7 (2000).
- [11] Dorn, R., Quabis, S. & Leuchs, G. Sharper focus for a radially polarized light beam. *Phys. Rev. Lett.* **91**, 233901 (2003).
- [12] Brown, T. G. Unconventional polarization states: Beam propagation, focusing, and imaging. In *Prog. Optics* **56** (Elsevier, London, 2011).
- [13] Niziev, V. G. & Nesterov, A. V. Influence of beam polarization on laser cutting efficiency. *J. Phys. D: Appl. Phys.* **32**, 1455–1461 (1999).
- [14] Meier, M., Romano, V. & Feurer, T. Material processing with pulsed radially and azimuthally polarized laser radiation. *Appl. Phys. A-Mater.* **86**, 329–334 (2007).
- [15] Mojarad, N. M. & Agio, M. Tailoring the excitation of localized surface plasmon-polariton resonances by focusing radially-polarized beams. *Opt. Express* **17**, 117–122 (2009).
- [16] Fatemi, F. K. Cylindrical vector beams for rapid polarization-dependent measurements in atomic systems. *Opt. Express* **19**, 25143–25150 (2011).
- [17] Kozawa, Y. & Sato, S. Optical trapping of micrometer-sized dielectric particles by cylindrical vector beams. *Opt. Express* **18**, 10828–10833 (2010).
- [18] Kindler (née Müller), J., Banzer, P., Quabis, S., Peschel, U. & Leuchs, G. Waveguide properties of single subwavelength holes demonstrated with radially and azimuthally polarized light. *Appl. Phys. B-Lasers O.* **89**, 517–520 (2007).
- [19] Neugebauer, M., Bauer, T., Banzer, P. & Leuchs, G. Polarization tailored light driven directional optical nanobeacon. *Nano Lett.* **14**, 2546–2551 (2014).
- [20] Woźniak, P., Banzer, P. & Leuchs, G. Selective switching of individual multipole resonances in single dielectric nanoparticles. *Laser Photonics Rev.* **9**, 231–240 (2015).
- [21] Souza, C., Huguenin, J., Milman, P. & Houry, A. Topological phase for spin-orbit transformations on a laser beam. *Phys. Rev. Lett.* **99**, 160401 (2007).
- [22] Holleczek, A., Aiello, A., Gabriel, C., Marquardt, C. & Leuchs, G. Poincaré sphere representation for classical inseparable Bell-like states of the electromagnetic field. arXiv preprint arXiv:1007.2528 (2010).
- [23] Borges, C. V. S., Hor-Meyll, M., Huguenin, J. A. O. & Houry, A. Z. Bell-like inequality for the spin-orbit separability of a laser beam. *Phys. Rev. A* **82**, 033833 (2010).
- [24] Karimi, E. *et al.* Spin-orbit hybrid entanglement of photons and quantum contextuality. *Phys. Rev. A* **82**, 022115 (2010).
- [25] Qian, X.-F. & Eberly, J. H. Entanglement and classical polarization states. *Opt. Lett.* **36**, 4110–2 (2011).
- [26] Kagalwala, K. H., Di Giuseppe, G., Abouraddy, A. F. & Saleh, B. E. A. Bell’s measure in classical optical coherence. *Nat. Photonics* **7**, 72–78 (2012).
- [27] Nielsen, M. A. & Chuang, I. L. *Quantum computation and quantum information*. (Cambridge University Press, Cambridge, 2000).
- [28] Aiello, A., Töppel, F., Marquardt, C., Giacobino, E. & Leuchs, G. Classical entanglement: Oxymoron or resource? arXiv preprint arXiv:1409.0213v2 (2014).
- [29] Gabriel, C. *et al.* Entangling different degrees of freedom by quadrature squeezing cylindrically polarized modes. *Phys. Rev. Lett.* **106**, 1–4 (2011).
- [30] de Oliveira, A. N., Walborn, S. P. & Monken, C. H. Implementing the Deutsch algorithm with polarization and transverse spatial modes. *J. Opt. B-Quantum S. O.* **7**, 288–292 (2005).
- [31] Hashemi Rafsanjani, S. M., Mirhosseini, M., Magaña-Loaiza, O. S. & Boyd, R. W. Teleportation via classical entanglement arXiv preprint arXiv:1503.03807v1 (2015).
- [32] Goyal, S. K., Roux, F. S., Forbes, A. & Konrad, T. Implementing quantum walks using orbital angular momentum of classical light. *Phys. Rev. Lett.* **110**, 263602 (2013).
- [33] Töppel, F., Aiello, A., Marquardt, C., Giacobino, E. & Leuchs, G. Classical entanglement in polarization metrology. *New J. Phys.* **16**, 073019 (2014).
- [34] Holleczek, A., Aiello, A., Gabriel, C., Marquardt, C. & Leuchs, G. Classical and quantum properties of cylindrically polarized states of light. *Opt. Express* **19**, 9714–9736 (2011).
- [35] Beckley, A. M., Brown, T. G. & Alonso, M. A. Full Poincaré beams. *Opt. Express* **18**, 10777–10785 (2010).
- [36] Kheifets, S., Simha, A., Melin, K., Li, T. & Raizen, M. G. Observation of brownian motion in liquids at short times: Instantaneous velocity and memory loss. *Science* **343**, 1493–1496 (2014).
- [37] Siegman, A. E. How to (Maybe) Measure Laser Beam Quality. *OSA TOPS* **17**, *Diode Pumped Solid State Lasers: Applications and Issues* (1998).
- [38] Siegman, A. E. *Lasers*. (University Science Books, Mill Valley, CA, 1986).
- [39] von Toussaint, U. Bayesian inference in physics *Rev. Mod. Phys.* **83**, 943–999 (2011).

SUPPLEMENTARY MATERIAL: POSITION TRACKING ALGORITHM

Here we explain the algorithm used to infer the transverse central coordinates (x_0, y_0) of a spherical object from measurements of the polarization Stokes parameters $\mathbf{s} = (s_0, s_1, s_2)$. Among the advantages of a numerical implementation are that experimental beam imperfections and electronic detector noise can be accounted for in a straightforward manner. Eqs. (7) in the “Methods” showed how to compute the individual Stokes parameters as a function of the transverse position of an object covering a known region \mathcal{A} . Before the actual sensing measurement, we perform this computation for each possible object position in discrete steps using the experimentally determined spatially resolved beam polarization tomographies $|P_\varphi \mathbf{E}(\boldsymbol{\rho}, z)|^2$, effectively yielding a look-up table $(x_0, y_0) \rightarrow \mathbf{s}$ as visualised by the surfaces in Figure 5a. By taking into account the normally distributed, experimentally determined statistical noise of each detector, the look-up table can be turned into a likelihood distribution $L(\mathbf{s}|(x_0, y_0))$. During the real-time sensing measurement, given a measured Stokes vector \mathbf{s} , the position can be inferred by finding the coordinates (x_0, y_0) maximizing this likelihood distribution (see Figure 5b).

The rotational symmetry of the radially polarized mode implies a twofold ambiguity in determining the object’s position, since rotating any object by 180° about the beam’s center leaves the Stokes parameters invariant. This ambiguity can be lifted by making a number of additional assumptions, such as specifying the half-plane where the particle is located at time $t = 0$ (initial position), and that its velocity is small compared to the sampling frequency (continuity of position), or that its acceleration stays within physically motivated bounds (continuity of velocity). Such assumptions can easily be accommodated within the framework of Bayesian probability theory (BPT) [39], where they take the role of *prior information*. BPT also assigns a formal role to other assumptions such as the size of the object to be tracked, and provides the means to estimate such parameters when they are not known *a priori*. However, in our laboratory setting we observe that the beam’s symmetry is already broken by small beam imperfections (including a slight, but not complete, four-fold symmetry in intensity). Interestingly, we found that taking into account this overall asymmetry helps to determine the trajectory unambiguously with high certainty without such additional assumptions as described before. If necessary, the symmetry could also be broken in more controlled ways, e.g. by introducing a second beam, or by using a beam with a less symmetric polarization structure [35].

We emphasize that the algorithm used is non-recursive and does not require any repeated iterations on the same data. Rather, it relies mainly on data which can be pre-computed in the form of look-up tables to any desired accuracy in a computationally efficient way. Hence, the algorithm is highly parallelizable and thus compatible with the requirements of high-speed real-time signal processing. The algorithm’s performance is rather insensitive to the assumed shape of the object: assuming a square of the same area instead of a circle leads to identical inferred positions (up to the width of the 68% credibility region). Changing the assumed object size generally leads to a radial shift of the inferred trajectory, but leaves the main features of the trajectory intact.

For the measurements shown here, we accounted for diffraction by assuming an effective sphere diameter at the detector plane which is 35% larger than the sphere’s actual physical dimensions. It is likely that the accuracy can be further increased by incorporating a more detailed model of diffraction. However, the actual impact of diffraction and the appropriate model to incorporate it will depend on the particular application under consideration.

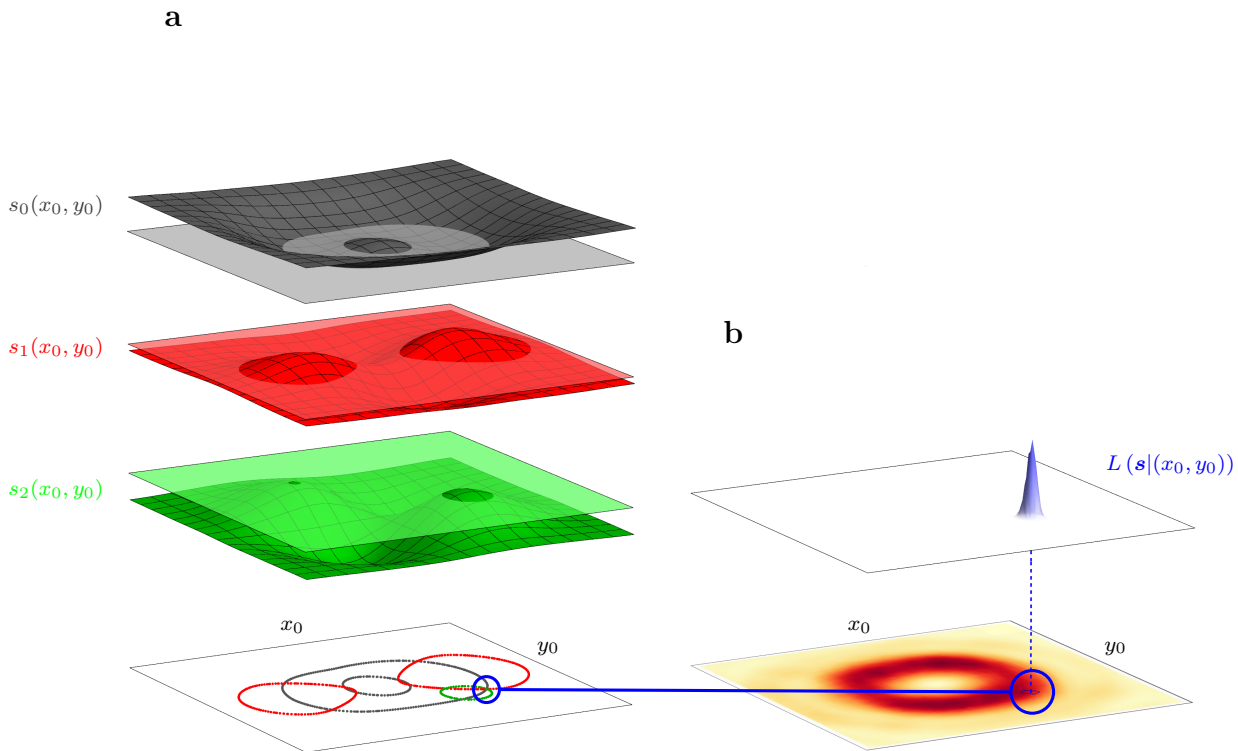


FIG. 5. **Position tracking (experimental data).** **a.** For a known beam and object geometry, a look-up table $(x_0, y_0) \rightarrow s_{\{0,1,2\}}$ may be computed from Eqs. (7), giving the expected Stokes parameters as a function of the object's transverse position within the beam. One such look-up table, obtained from experimental data, is visualized here as a set of three surfaces. The measurement of a particular Stokes vector may be regarded as a set of planes intersecting these surfaces. The intersection of the corresponding contours (shown on the bottom) indicates the position of the object. **b.** The upper plane shows the likelihood distribution $L(\mathbf{s}|(x_0, y_0))$ for the measured Stokes vector \mathbf{s} . The maximum of this distribution corresponds to the inferred position. Note that although the theory for an ideal mode predicts two solutions, this symmetry may be broken in practice due to slight irregularities in the mode pattern, as demonstrated by this particular example.